

Journal of Materials Chemistry C

Accepted Manuscript



This is an *Accepted Manuscript*, which has been through the Royal Society of Chemistry peer review process and has been accepted for publication.

Accepted Manuscripts are published online shortly after acceptance, before technical editing, formatting and proof reading. Using this free service, authors can make their results available to the community, in citable form, before we publish the edited article. We will replace this *Accepted Manuscript* with the edited and formatted *Advance Article* as soon as it is available.

You can find more information about *Accepted Manuscripts* in the [Information for Authors](#).

Please note that technical editing may introduce minor changes to the text and/or graphics, which may alter content. The journal's standard [Terms & Conditions](#) and the [Ethical guidelines](#) still apply. In no event shall the Royal Society of Chemistry be held responsible for any errors or omissions in this *Accepted Manuscript* or any consequences arising from the use of any information it contains.

Low thermal conductivity and rapid synthesis of n-type cobalt skutterudite via hydrothermal method

Ahmad Gharleghi, Yi-Hsuan Pai, Fei-Hung Lin, and Chia-Jyi Liu*

*e-mail: liucj@cc.ncue.edu.tw

Department of Physics, National Changhua University of Education, Changhua 500,
Taiwan.

Abstract

We report low thermal conductivity for n-type cobalt skutterudites synthesized via a rapid hydrothermal procedure combined with evacuated-and-encapsulated heating. Different synthesis temperatures are investigated to obtain the single phase of CoSb₃. The resulting samples are characterized using x-ray diffraction pattern, scanning electron microscopy, Hall and density measurements. A remarkably low thermal conductivity of 1.33 - 1.46 Wm⁻¹K⁻¹ at room temperature can be attained for the pristine CoSb₃, which is comparable with or even lower than the filled CoSb₃ obtained from solid state reaction. Regarding the requirement of lengthy annealing and reaction at high temperature using solid state reaction, our remarkably rapid and low temperature procedure fabrication together with the significantly low thermal conductivity presents major progress in fabricating cobalt skutterudites using hydrothermal synthesis methods.

Keyword: Rapid Synthesis, Hydrothermal Methods, Cobalt Skutterudite, Thermal Conductivity, Thermoelectric Properties.

1. Introduction

Waste energy recovery via novel technologies such as thermoelectric generators has recently received great attention especially due to wane of petroleum resources and environmental pollution problems. Energy harvesting from the exhaust heat for practical applications is feasible by using thermoelectric devices. The efficiency of a thermoelectric material is evaluated from its figure of merit $zT = \sigma S^2 T / \kappa$, where S is the thermopower (Seebeck coefficient), σ is the electrical conductivity, κ the thermal conductivity, and T the absolute temperature.

Among potential thermoelectric materials, skutterudites have attracted great research interests.¹ Skutterudites with TPn_3 ($T = \text{Co, Rh, or Ir}$ and $Pn = \text{P, As, or Sb}$) structure crystalize in the cubic lattice of CoAs_3 -type with space group $\text{Im}\bar{3}$.² CoAs_3 -type structures possess two intrinsic voids per unit cell. The voids especially for the CoSb_3 skutterudite are large enough to accommodate guest ions of alkaline earth or rare earth elements as filled skutterudites.^{3,4} The rattling motion of the filler atoms inside the Sb-icosahedral voids could decrease the lattice thermal conductivity by broadening the spectrum of scattered phonon modes.⁵ One of the objectives for

lowering the lattice thermal conductivity of skutterudites is to reduce the $Im\bar{3}$ (T_h^5) space group symmetry by distorting the pnictogen ring (Sb-ring) via substituting Pn ion with Ge, Sn, Te or Se elements.^{4,6-9}

Nanostructured fabrication has been proven an effective approach to reduce lattice thermal conductivity. It is a common practice now to reduce the lattice thermal conductivity through scattering heat-carrying phonons at interfaces by introducing nanoparticles in the matrix. Based on the Callaway formalism, the effect of particle size on the lattice thermal conductivity can be described in terms of the phonon relaxation rates as¹⁰⁻¹²

$$\tau_C^{-1} = \tau_U^{-1} + \tau_N^{-1} + \tau_{p-d}^{-1} + \tau_{e-ph}^{-1} + \tau_b^{-1}, \quad (1)$$

where C denotes combined scattering rate, U , N , $p-d$, $e-ph$, and b represent phonon umklapp processes, phonon Normal, point-defect, electron-phonon, and boundary, respectively. Phonon scattering rate on the boundaries depends on the grain size as $\tau_b^{-1} = 3xv_s/2R$; where x , v_s , and R are the content of nanoparticles in the matrix, the speed of sound, and nanoparticle size, respectively.¹³ The shape and size of nanoparticles (R), and their content are some crucial parameters in phonon scattering rate. Therefore the fabrication condition plays an important role in reducing thermal

conductivity with the objective to enhance zT values. Developing nanostructured thermoelectric materials in minimizing heat transport without deteriorating the electrical properties may require fine tuning the synthetic conditions. A good nanostructured thermoelectric material needs to possess endotaxial characteristic.^{9,14} The endotaxially dispersed nanoparticles need to be coherent with embedded fine-grains in their vicinity.

Preparation cost also receives special attention as one of the key factors in evaluating the thermoelectric materials for practical usages. Developing synthesis procedure with short duration would be one of the objectives to reduce the fabrication costs. Recently, Uher et al. have reported a rapid procedure for producing cobalt skutterudite using the melt spinning method, which takes about 20 h.¹⁵ Their method is promising for practical application as compared with those traditional solid state reaction methods that usually requires long annealing time of 7 to 10 days.¹⁶⁻¹⁹ We have recently reported a rapid synthesis of cobalt skutterudite using modified polyol process.²⁵ However, there are some disadvantages of the polyol methods. The triethylene glycol (TEG) used as the solvent in polyol synthesis is costly; the synthesized powders requires 750 ml ethanol to rinse off viscous TEG. Besides, in the course of polyol synthesis, it requires special attention to avoid the formation of Sb_2O_3 . Compared with solid state reaction methods, the hydrothermal synthesis

process is not particularly common for fabricating CoSb_3 .²⁰ In this work we have developed a hydrothermal synthesis procedure to produce CoSb_3 compound at low temperatures. Various hydrothermal synthesis temperatures with a short duration of 12 h are investigated aiming at finding optimum condition of producing pure CoSb_3 phase. As a result, we are able to obtain nearly single phase of CoSb_3 at the synthesis temperature of 290°C using the hydrothermal method for the first time. For those synthesized at lower temperatures, it requires heating hydrothermally synthesized powders at 580°C for a short period of 5 h in an evacuated-and-encapsulated ampoule. In particular, all these samples exhibit low thermal conductivity ranging from $1.33 \text{ Wm}^{-1}\text{K}^{-1}$ to $1.46 \text{ Wm}^{-1}\text{K}^{-1}$. The thermal conductivity reported for the pristine CoSb_3 synthesized from solid state reaction methods falls in the range of 3 and $10 \text{ Wm}^{-1}\text{K}^{-1}$ at room temperature.^{2, 21-23} Yang et al. reported a low thermal conductivity of $1.94 \text{ Wm}^{-1}\text{K}^{-1}$ around room temperature for nano-sized p-type CoSb_3 synthesized using modified polyol process.²⁴

2. Experimental Procedure

Cobalt skutterudites CoSb_3 were synthesized using hydrothermal methods. Powders of SbCl_3 and $\text{CoCl}_2 \cdot 6\text{H}_2\text{O}$ were weighted and loaded into a Teflon cup (~185 mL volume) containing 110 mL deionized water. For the present container volume

and solvent amount, 10.65 millimole SbCl_3 and required amount of $\text{CoCl}_2 \cdot 6\text{H}_2\text{O}$ (with Sb:Co ratio 3:1) was used. The solution was then sonicated at 47°C for 30 min, followed by adding 74.26 millimole of NaOH and sonicated for another 15 min. To create a reductive environment, 78.56 millimole NaBH_4 was added to above solution, followed by sonication at 47°C for 30 min and then loaded into an autoclave and heated in an oven with heating rate of $2.6^\circ\text{C}/\text{min}$ at various temperatures for 12 h. The resulting product was then washed using ethanol and deionized water. Drying of the powders was carried out using a rotary evaporator vacuum dryer. To avoid oxidation of as-synthesized powders, the Ar gas was used to purge the flask before drying and introduced into the flask while breaking the vacuum after drying. The dried powders were then cold-pressed at 16.88 MPa to form a parallelepiped. The prepared parallelepiped was then loaded into a Pyrex ampoule, which was evacuated using a diffusion pump to reach 10^{-5} Torr to 10^{-6} Torr and then sealed.²⁶ The parallelepiped in the encapsulated ampoule was then heated in a tubular furnace at a rate of $2.6^\circ\text{C}/\text{min}$ to 580°C , and hold for 5 h. The phase identification of as-synthesized powders and as-sintered samples was carried out using a Shimadzu XRD-6000 diffractometer equipped with Fe $K\alpha$ radiation. The morphology of the samples was examined using a Zeiss AURIGA field emission scanning electron microscope (FE-SEM). Electrical resistivity and thermopower measurements were

simultaneously carried out from room-temperature down to liquid nitrogen temperature. Thermopower measurements were carried out using steady-state techniques. A type E differential thermocouple connected to a Keithley 2000 multimeter was used to measure the temperature difference between the hot and cold ends of the sample. The thermally generated Seebeck voltage across the sample was measured using a Keithley 2182 nanovoltmeter.²⁷ The thermopower of sample was obtained by subtracting the thermopower of the Cu. Electrical resistivity measurements were performed using standard four-probe techniques, reversing the current sources to cancel thermoelectric voltages. Thermal conductivity measurements were carried out using transient plane source techniques with very small temperature perturbations of the sample material by the Hot Disk thermal constants analyzer as described in detail elsewhere.²⁶ The uncertainty for the electrical resistivity, thermopower, and thermal conductivity is about $\pm 3\%$, $\pm 4\%$ and $\pm 4\%$, respectively. Hall measurements was performed using the van der Pauw method under an applied magnetic field of 0.55 T (ECOPIA:HMS -3000). The relative density of all the samples was measured using the Archimedes' method.

3. Results and Discussion

Fig. 1 shows the x-ray diffraction (XRD) patterns of the as-synthesized CoSb_3

powders at 170°C, 230°C, and 290°C, respectively. The phase evolution of CoSb, CoSb₂ and CoSb₃ can be readily seen for hydrothermal reaction carried out at various temperatures. The samples synthesized at 170°C shows CoSb and Sb as the major phases. At the synthesized temperature of 230°C, the desired phase of CoSb₃ coexists with CoSb₂, CoSb, and Sb. Nearly single phase of CoSb₃ can be obtained at 290°C. The CoSb₃ phase, however, can be achieved by heating the powders, which are synthesized below 290°C, in evacuated-and-encapsulated ampoules at 580°C for a short period of 5 hours. Fig. 2 displays the powder XRD patterns of all the as-heated samples. It can be seen that all the samples exhibit the CoSb₃ phase as the major phase with tiny amount of CoSb₂. The lattice constant is refined from the XRD data for all the three samples. The obtained values are 9.030(2), 9.034(2), and 9.038(2) Å for samples synthesized at 170°C, 230°C, and 290°C, respectively, which are in good agreement with other reports for the title system.^{2,28}

Fig. 3 shows the FE-SEM micrographs from fractured samples heated at 580°C and synthesized at 170°C (Fig. 3a) and 290°C (Fig. 3b), respectively. Porosity and various grain sizes in the range of 30 and 200 nm can be readily seen. The bulk density of all the three samples is measured about 71 to 78 % of the theoretical density (Table I), indicating porous nature as seen in Fig. 3. The carrier concentration and mobility obtained from Hall measurements at room temperature are presented in

Table I. The results of these measurements confirm that electrons are the majority charge carriers for all the samples. The low electron mobility might be associated with their porous microstructures and relatively small particle sizes.

Now we turn to the effects of synthetic condition on the transport properties. Fig. 4 shows the temperature dependence of electrical conductivity from 300 K down to liquid nitrogen temperature for samples synthesized at various temperatures of 170°C, 230°C and 290°C. The electrical conductivity decreases with decreasing temperature for all the samples. Fig. 5 displays the temperature dependence of thermopower from room temperature down to liquid nitrogen temperature for samples synthesized at various temperatures of 170°C, 230°C, and 290°C. Negative thermopower observed for all the samples indicates that electrons are the majority charge carriers, being consistent with the Hall measurements (Table I). The absolute value of thermopower decreases with decreasing temperature for all the samples. The sample synthesized at 290°C displays the smallest absolute value of thermopower among all the samples within the whole measured temperature range, while the one synthesized at 170°C displays the largest magnitudes of thermopower in the whole measured temperature range. By assuming acoustic phonons as predominant electron scattering resources for materials with a single parabolic conduction band, the thermopower and carrier concentration can be respectively expressed as²⁹⁻³¹

$$S = \pm \frac{k_B}{e} \left(2 \frac{F_1(\eta)}{F_0(\eta)} - \eta \right) \text{ and} \quad (2)$$

$$n = \frac{4}{\sqrt{\pi}} (2\pi m^* k_B T / h^2)^{3/2} F_{\frac{1}{2}}(\eta), \quad (3)$$

where $\eta = E_F / k_B T$ is the reduced Fermi energy, F_j the Fermi-Dirac integrals of order j , k_B is the Boltzmann's constant, h Planck's constant, and m^* the electron effective mass. By substituting the room-temperature thermopower and carrier concentrations values (Table I) together with the tabulated magnitudes for Fermi-Dirac integrals in Eq.(2) and (3), η and m^* are estimated for all the three CoSb₃ samples and results are presented in Table I. The reduced Fermi level is measured from the conduction band edge, and the largest η value of -1.8 is obtained for the sample that was synthesized at 170°C. The estimated η values show that the Fermi level moves towards the conduction band edge by increasing the carrier concentration. The effective mass is extended around the free electron mass m_o with the largest value of about 1.11 m_o for the sample synthesized at 170°C (Table I). The number of energy states at the conduction band edge can be estimated by inserting the effective mass into the effective density of states $2(2\pi m^* k_B T / h^2)^{3/2}$; the derived values is on the order of 10^{19} cm⁻³ and directly rely on the m^* values for all the three samples (Table I).

The similar curves of both electrical conductivity and thermopower with respect

to temperature might indicate similar conduction mechanism governing the electronic transport for all the three samples. The electrical conductivity for the three samples (Fig. 4) reduces at a faster rate with decreasing temperature in the higher temperature regime ($238 \leq T \leq 300$ K) when compared with that in the lower temperature regime ($77 \leq T \leq 130$ K). Therefore, the activation type conduction mechanism at higher temperatures and the Mott's $T^{1/4}$ law at the lower temperatures might be responsible for the dominant conduction mechanisms of the title CoSb_3 samples. To get insight of probably dominated conduction mechanism, the electrical conductivity curves at $238 \leq T \leq 300$ K and $77 \leq T \leq 130$ K is fitted with the Arrhenius relation and Mott's model, respectively,^{32,33}

$$\sigma(T) = \sigma_o \exp\left(-\frac{E_a}{k_B T}\right) \quad \text{and} \quad (4)$$

$$\sigma(T) = \sigma_o \exp\left[\left(-\frac{T_o}{T}\right)^{1/4}\right], \quad (5)$$

where σ_o is the pre-exponential constant, E_a the activation energy, the characteristic temperature $T_o = \beta \alpha^3 / (k_B N_F)$, β a constant, α^{-1} the decay length of the localized state wave function, and N_F the density of hopping states at the Fermi level. The fitted results are shown in Figs. 6 and 7. The energy band gap ($E_g = 2E_a$) of each sample is

calculated from the slopes of the $\text{Ln}(\sigma)$ versus T^{-1} curves and presented in Table I. The obtained E_g for the three samples synthesized at 170°C, 230°C, and 290°C is about 73, 81.8, and 83.6 meV, respectively. These values are in agreement with the theoretical computations for direct and pseudo band gap magnitudes for the CoSb_3 cell.^{34,35} As all the three E_g values are larger than $k_B T$ for $T \leq 300$ K, applying the Mott's theory of variable-range hopping (VRH) at $77 \leq T \leq 130$ K for the title samples should be acceptable.³³ It can be also seen that the electrical conductivity for all the three samples obeys the Mott's VRH conduction model at $77 \leq T \leq 130$ K. These results might indicate that the conduction is dominated by variable range hopping process. Based on the decreasing absolute values of thermopower with decreasing temperature for all the three samples, the temperature dependence of thermopower can also be expressed as^{36,37}

$$S = \frac{k_B}{2e} \frac{W^2}{k_B T} \left(\frac{d \ln N(E)}{dE} \right)_{E=E_F}, \quad (6)$$

where W is the hopping energy, $N(E)$ density of hopping states, and E_F the Fermi level.

In the framework of VRH process, $W \sim k_B (T_0 T^3)^{1/4}$, and the temperature dependence of thermopower in Eq. (6) can be expressed more clearly as

$$S = \frac{1}{2e} k_B^2 (T_o T)^{\frac{1}{2}} \left(\frac{d \ln N(E)}{dE} \right)_{E=E_F}, \quad (7)$$

The thermopower curves of all the three samples in Fig. 5 are fitted with $T^{1/2}$ using Eq. (7) for the same temperature region as in the electrical conductivity curve fitting (Fig. 7). Fig. 8 shows that the absolute value of thermopower increases linearly with $T^{1/2}$ for $77 \leq T \leq 130$ K. For the Mott's model of hopping conduction to be applicable for the title system, the energy independency of density of hopping states near the Fermi level is assumed.³⁹ Based on the fitting results for both the electrical conductivity and thermopower, we assume the variable range hopping is the dominate conduction mechanism for as-synthesized CoSb₃ samples at $77 \leq T \leq 130$ K. By inserting the obtained T_o values from the fitted curves of Fig. 7 into Eq.(7) together using the slope obtained from thermopower fitting in Fig. 8, we can estimate the magnitude of the hopping energy W and derivative of the logarithmic density of hopping states at the Fermi level, $\left[\frac{d \ln N(E)}{dE} \right]_{E=E_F}$. The hopping energy at T=100 K is calculated and presented in Table II.

Fig. 9 shows the temperature dependence of power factor, $PF = \sigma S^2$, for all the CoSb₃ samples synthesized at various temperatures. It can be readily seen that the largest power factor value of 0.72 $\mu\text{W}/\text{cm}\cdot\text{K}^2$ is attained at 300 K for the sample synthesized at 170°C. The power factor of all the samples turns smaller and levels off

to low values at about 77 K.

Fig. 10 shows the temperature dependence of the total thermal conductivity (κ) for the CoSb₃ samples. The room-temperature thermal conductivity for the samples synthesized at 170°C, 230°C, and 290°C is 1.34 Wm⁻¹K⁻¹, 1.46 Wm⁻¹K⁻¹, and 1.33 Wm⁻¹K⁻¹, respectively. The room-temperature thermal conductivity is markedly smaller than those reported for the parent CoSb₃ system.^{2,21,40} In addition, the low thermal conductivity of our samples is also comparable with or even lower than that of doped, filled, or nanostructured CoSb₃ prepared using solid state reaction.^{9,39-43}

The thermal conductivity increases with decreasing temperature for all the three samples, which might arise from increasing phonon mean free path upon cooling.⁴⁴ The thermal conductivity at 122 K is 2.95 Wm⁻¹K⁻¹ for the sample synthesized at 230°C. The electronic component of the thermal conductivity κ_e can be obtained using the Wiedemann-Franz law $\kappa_e/\sigma = LT$, where σ being the electrical conductivity and L the Lorenz number. The Lorenz number can be expressed as a functional Fermi-Dirac integrals, $F_j(\eta)$, as Eq. (8)^{2,29,30}

$$L = \left(\frac{k_B}{e}\right)^2 \left[\frac{3F_0(\eta)F_2(\eta) - 4F_1^2(\eta)}{F_0^2(\eta)} \right], \quad (8)$$

The magnitude of L for all the three samples is estimated using the tabulated

amounts for Fermi-Dirac integrals and the results are presented in Table I. The obtained L values show that the Lorenz number is slightly increased by decreasing the magnitude of η . By inserting the estimated L value into the Wiedemann-Franz law, we have calculated κ_e component and the related results is displayed in Fig. 11a. These results indicate that the electronic contribution to the thermal conductivity is quite small for all the three samples due to their relatively small electrical conductivity. The largest and smallest room-temperature κ_e is $2.65 \times 10^{-3} \text{ Wm}^{-1}\text{K}^{-1}$ and $2.41 \times 10^{-3} \text{ Wm}^{-1}\text{K}^{-1}$ for the samples synthesized at 290°C and 230°C , respectively. The κ_e component decreases with decreasing temperature for all the three samples such that its value at 122 K is about 5-times smaller than the related amount at 300 K. The lattice component of thermal conductivity (κ_L) is obtained by subtracting κ_e from the total thermal conductivity ($\kappa_L = \kappa - \kappa_e$) and shown in Fig. 11b. It can be readily seen that the total thermal conductivity κ mostly comes from the lattice contribution. While the correlation between κ_L and temperature indicates the characteristics of crystalline solids with dominate phonon contribution to the thermal conductivity, efforts for modeling the lattice contribution solely with umklapp phonon-phonon scattering did not show acceptable fitting. For the present CoSb_3 structure, assumption of combined-scattering process seems more reasonable, especially for $T \leq 240$ K. According to Callaway,⁴⁵ the lattice thermal conductivity can be expressed as

$$\kappa_L = \frac{k_B}{2\pi^2 v_s} \left(\frac{k_B T}{\hbar}\right)^3 \int_0^{\theta_D/T} \frac{y^4 e^y}{\tau_C^{-1} (e^y - 1)^2} dy, \quad (9)$$

where $y = \hbar \omega / k_B T$ is dimensionless parameter of integration, ω the phonon frequency, θ_D the Debye temperature, v_s the velocity of sound, and τ_C^{-1} the combined phonon scattering rate. Recalling Eq.(1) and ignoring the normal phonon scattering rate, τ_N^{-1} , the τ_C^{-1} in Eq. (9) can be expressed as follows^{21,45}

$$\tau_C^{-1} = AT\omega^2 \exp\left(-\frac{\theta_D}{aT}\right) + B\omega^4 + C\omega^2 + 3xv_s/2R, \quad (10)$$

where A , B , and C are constants, and a equal to about 2.⁴⁸ The terms in Eq. (10) represents umklapp phonon-phonon scattering, point-defect scattering, electron-phonon scattering, and grain boundary scattering rates, respectively. The parameter x and the particle size R are already explained in Eq. (1). Since the temperature region in our collected data is not that low for grain boundary scattering to dominate the lattice thermal conductivity of the title CoSb_3 samples, the main contribution might well be associated with the umklapp phonon-phonon scattering, point-defect scattering, and electron-phonon scattering at $122 \leq T \leq 300$ K. Similar thermal conductivity behavior associated with the mixed phonon scattering

mechanism has been reported for the CoSb_3 system at the same temperature region.^{21,44}

The thermoelectric figure-of-merit zT is calculated using the values of the power factor (σS^2) and the total thermal conductivity obtained for all the three samples and is shown in Fig. 12. The largest zT magnitude of about 0.016 is attained at 300 K for the sample synthesized at 170°C , which is comparable with earlier reports for the pristine CoSb_3 system.^{42,47,48} The room-temperature zT for the samples synthesized at 230°C and 290°C display almost the same value of about 0.008. For all the three samples, the zT decreases with decreasing temperature.

4. Conclusion

Rapid synthesis of n-type CoSb_3 can be achieved using hydrothermal methods combined with evacuated-and-encapsulated sintering. The pure CoSb_3 phase can be attained at 290°C for the duration of 12 h. The phase impurities for samples synthesized at lower temperatures can be removed by heating at 580°C for a short period of 5 h in an evacuated-and-encapsulated ampoule. The electrical conductivity data are analyzed to facilitate the understanding of the dominate conduction mechanism for hydrothermally synthesized CoSb_3 . It is found that the activated type conduction dominates for $238 \leq T \leq 295$ K. The variable-range hopping model of

conduction can be well fitted to both the electrical conductivity and thermopower curves for $77 \leq T \leq 130$ K. The thermal conductivity displays remarkably low room-temperature values for all the three CoSb_3 samples. The lowest room-temperature lattice thermal conductivity is about $1.33 \text{ Wm}^{-1}\text{K}^{-1}$ for the sample synthesized at 290°C , which by comparison is as low as the filled cobalt skutterudite compounds. The largest zT of 0.016 is attained at room temperature for the sample synthesized at 170°C .

Acknowledgments

This work is supported by the National Science Council of Taiwan, ROC, grant No. NSC 101-2112-M-018-003-MY3.

References

- 1 Lan, Y.; Minnich, A. J.; Chen, G.; Ren, Z. *Adv. Funct. Mater.*, 2010, **20**, 357.
- 2 Caillat, T.; Borshchevsky, A.; Fleurial, J. P. *J. Appl. Phys.*, 1996, **80**, 4442.
- 3 Uher, C. In: *Recent Trends in Thermoelectric Materials Research I, Semiconductors and Semimetals*, 2001, 69, Ch. 5, 139-253, edited by: Tritt, T. M. (Academic Press).
- 4 Chi, H.; Kim, H.; Thomas, J. C.; Su, X.; Stackhouse, S.; Kaviani, M.; Van der Ven, A.; Tang, X.; Uher, C. *Phys. Rev. B*, 2012, **86**, 195209.
- 5 Nolas, G. S.; Kendziora, C. A.; Takizawa, H. *J. Appl. Phys.*, 2003, **94**(12), 7440-4.
- 6 Liu, W. S.; Zhang, B. P.; Zhao, L. D.; Li, J. F. *Chem. Mater.*, 2008, **20**, 7526–7531.
- 7 Su, X.; Li, H.; Wang, G.; Chi, H.; Zhou, X.; Tang, X.; Zhang, Q.; Uher, C. *Chem. Mater.*, 2011, **23**, 2948-2955.
- 8 Su, X.; Li, H.; Yan, Y.; Chi, H.; Tang, X.; Zhang, Q.; Uher, C. *J. Mater. Chem.*, 2012, **22**, 15628–15634.
- 9 Su, X.; Li, H.; Yan, Y.; Wang, G.; Chi, H.; Zhou, X.; Tang, X.; Zhang, Q.; Uher, C. *Acta. Materialia.*, 2012, **60**, 3536–3544.
- 10 Callaway, J.; von Baeyer, H. C. *Phys. Rev.*, 1960, **120**, 1149.
- 11 Steigmeier, E. F.; Abeles, B. *Phys. Rev.*, 1964, **136**, A1149.
- 12 Lee, H.; Vashaee, D.; Wang, D. Z.; Dresselhaus, M. S.; Ren, Z. F.; Chen, G. J. *Appl. Phys.*, 2010, **107**, 094308.

- 13 Sergey V. F.; Francois, L. *Phys. Rev. B*, 2008, **77**, 214304.
- 14 Vineis, C. J.; Shakouri, A.; Majumdar, A.; Kanatzidis, M. G. *Adv. Mater.*, 2010, **22**, 3970–3980.
- 15 Tan, G.; Liu, W.; Wang, S.; Yan, Y.; Li, H.; Tang, X.; Uher, C. *J. Mater. Chem. A*, 2013, **1**, 12657.
- 16 Yang, J.; Chen, Y.; Peng, J.; Song, X.; Zhu, W.; Su, J.; Chen, R. *J. Alloys. Compd.*, 2004, **375**, 229.
- 17 Geng, H. Y.; Ochi, S.; Guo, J. Q. *Appl. Phys. Lett.*, 2007, **91**, 022106.
- 18 Katsuyama, S.; Watanabe, M.; Kuroki, M.; Maehata, T.; Ito, M. *J. Appl. Phys.*, 2003, **93**, 2758.
- 19 Tan, G.; Wang, S.; Tang, X.; Li, H.; Uher, C. *Chem.*, 2012, **196**, 203.
- 20 Du, Y.; Cai, K. F.; Chen, S.; Qin, Z.; Shen, S. Z. *J. Electron. Mater.*, 2011, **40**, 5.
- 21 Yang, J.; Morelli, D. T.; Meisner, G. P.; Chen, W.; Dyck, J. S.; Uher, C. *Phys. Rev. B*, 2002, **65**, 094115.
- 22 Yang, J.; Meisner, G. P.; Morelli, D. T.; Uher, C. *Phys. Rev. B*, 2000, **63**, 014410.
- 23 Park, K. H.; Kim, I. H. *J. Electron. Mater.*, 2011, **40**(5).
- 24 Yang, L.; Hng, H. H.; Li, D.; Yan, Q. Y.; Ma, J.; Zhu, T. J.; Zhao, X. B.; Huang, H. *J. Appl. Phys.*, 2009, **106**, 013705.
- 25 Gharleghi, A.; Liu, C.-J. *J. Alloys. Compd.*, 2014, **592**, 277.

- 26 Liu, C.-J.; Lai, H.-C.; Liu, Y.-L.; Chen, L.-R. *J. Mater. Chem.*, 2012, **22**, 4825.
- 27 Liu, C. J.; Huang, Y. C.; Nong, N. V.; Liu, Y. L.; Petricek., V. *J. Electron. Mater.*, 2011, **40** (5).
- 28 Kjekshus, A.; Rakke, T. *Acta Chem. Scand.*, A 1974, **28**, 99.
- 29 Goldsmid, H. J. *Electronic Refrigeration*, 1986 (Pion Limited, London).
- 30 Anno, H.; Matsubara, K.; Notohara, Y.; Sakakibara, T.; Tashiro, H. *J. Appl. Phys.*, 1999, **86**, 7, 3780.
- 31 Dyck, J. S.; Chen, W.; Yang, J.; Meisner, G. P.; Uher, C. *Phys. Rev. B*, 2002, **65**, 115204.
- 32 Mott, N. F. *J. Non-Cryst. Solids*, 1968, **1**, 1-17.
- 33 Brodsky, M. H.; Kaplan, D. J. *Non-Cryst. Solids*, 1979, **32**, 431.
- 34 Singh, D. J.; Pickett, W. E. *Phys. Rev. B*, 1994, **50**, 11 235.
- 35 Puyet, M.; Lenoir, B.; Dauscher, A.; Pécheur, P.; Bellouard, C.; Tobola, J.; Hejtmanek, J. *Phys. Rev. B*, 2006, **73**, 035126.
- 36 Chakrabarti, B.; Chaudhuri, S.; Pal, A. K. *Jpn. J. Appl. Phys.*, 1983, **22**, 903.
- 37 Cutler, M.; Mott, N. F. *Phys. Rev.*, 1969, **181**, 1336.
- 38 Mott, N. F. *Electronic and Structural Properties of Amorphous Semiconductors*, 1973 (eds. Lecomber, P. G., & Mort, J.) 1 (Academic Press, London).
- 39 Chen, L. D.; Kawahara, T.; Tang, X. F.; Goto, T.; Hirai, T.; Dyck, J. S.; W. Chen,

- Uher, C. J. Appl. Phys., 2001, **90**, 1864.
- 40 Toprak, M. S.; Stiewe, C.; Platzek, D.; Williams, S.; Bertini, L.; Muller, E.; Gatti, C.; Zahang, Y.; Powe, M.; Muhammed, M. Adv. Funct. Mater., 2004, **14**, 1189.
- 41 Li, H.; Tang, X.; Zhang, Q.; Uher, C. Appl. Phys. Lett., 2009, **94**, 102114.
- 42 Sales, B. C.; Chakoumakos, B. C.; Mandrus, D. Phys. Rev. B, 2000, **61**, 2475.
- 43 Yang, J.; Zhang, W.; Bai, S. Q.; Mei, Z.; Chen, L. D. Appl. Phys. Lett., 2007, **90**, 192111.
- 44 Morelli, D. T.; Caillat, T.; Fleurial, J. P.; Borshchevsky, A.; Vandersande, J.; Chen, B.; Uher, C. Phys. Rev. B, 1995, **51**, 9622.
- 45 Callaway, J. Phys. Rev., 1959, **113**, 1046.
- 46 Goldsmid, H. J. Introduction to Thermoelectricity, 2010, p. 38 (Springer Series in Materials Science, Verlag Berlin Heidelberg).
- 47 Mallik, R. C.; Anbalagan, R.; Raut, K. K.; Bali, A.; Royanian, E.; Bauer, E.; Rogl, G.; Rogl, P. J. Phys.: Condens. Matter, 2013, **25**, 105701.
- 48 Sharp, J. W.; Jones, E. C.; Williams, R. K.; Martin, P. M.; Sales, B. C. J. Appl. Phys., 1995, **78**, 1013-8.

Figure Captions

Fig. 1, Powder XRD pattern of hydrothermally reacted samples at various temperatures (insets) for 12 h. Herein hkl indices denote CoSb_3 phase, (+), (*) and (\$) symbols represent CoSb_2 , CoSb and Sb impurity phases, respectively.

Fig. 2, Powder XRD patterns of as-hydrothermally reacted samples (Fig. 1) after heating at 580°C for 5 h into evacuated ampoules; thereat hkl indices denote CoSb_3 phase and (+) symbol represents CoSb_2 impurity phase.

Fig. 3, SEM micrographs from the polished surface of samples hydrothermally synthesized at (a) 170°C and (b) 290°C for duration of 12 h, followed by heating at 580°C for 5 h into evacuated ampoules.

Fig. 4, Electrical conductivity of CoSb_3 samples hydrothermally synthesized at various temperatures (inset of figure) followed by heating into evacuated ampoules at 580°C for 5 h.

Fig. 5, Thermopower of CoSb_3 samples hydrothermally synthesized at various temperatures (inset of figure) followed by heating into evacuated ampoules at 580°C

for 5 h.

Fig. 6, Plot of $\text{Ln}\sigma$ versus T^{-1} for CoSb_3 samples hydrothermally synthesized at various temperatures (inset); the activation energies are calculated using the slopes.

Fig. 7, Plot of $\text{Ln}\sigma$ versus $T^{-1/4}$ in the framework of the Mott's variable-range hopping model for CoSb_3 samples hydrothermally synthesized at various temperatures (inset).

Fig. 8, Plot of thermopower versus $T^{1/2}$ in the framework of the Mott's variable-range hopping model for the CoSb_3 samples hydrothermally synthesized at various temperatures (inset).

Fig. 9, Power Factor for CoSb_3 samples hydrothermally synthesized at various temperatures (inset) followed by heating into evacuated ampoules at 580°C for 5 h.

Fig. 10, Total thermal conductivity (κ) of CoSb_3 samples hydrothermally synthesized at various temperatures (inset of figure) followed by heating into evacuated ampoules at 580°C for 5 h.

Fig. 11, (a) Electronic component (κ_e) and (b) the lattice component ($\kappa_L = \kappa - \kappa_e$) of

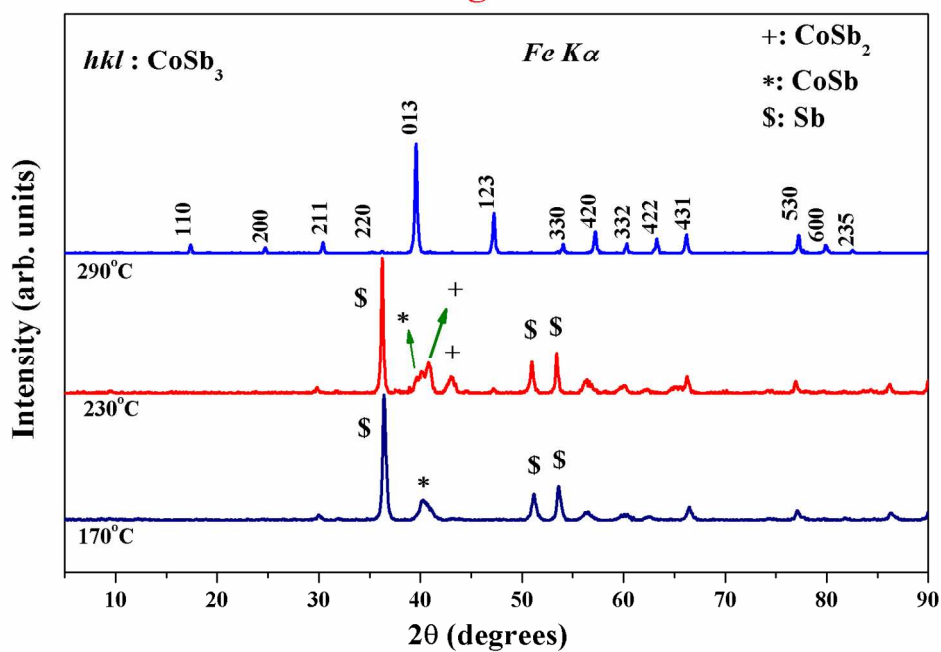
the total thermal conductivity (κ) calculated for the title CoSb₃ samples.

Fig. 12, Figure-of-merit, zT , attained for CoSb₃ samples hydrothermally synthesized at various temperatures (inset) followed by heating at 580°C for 5 h.

Table Captions

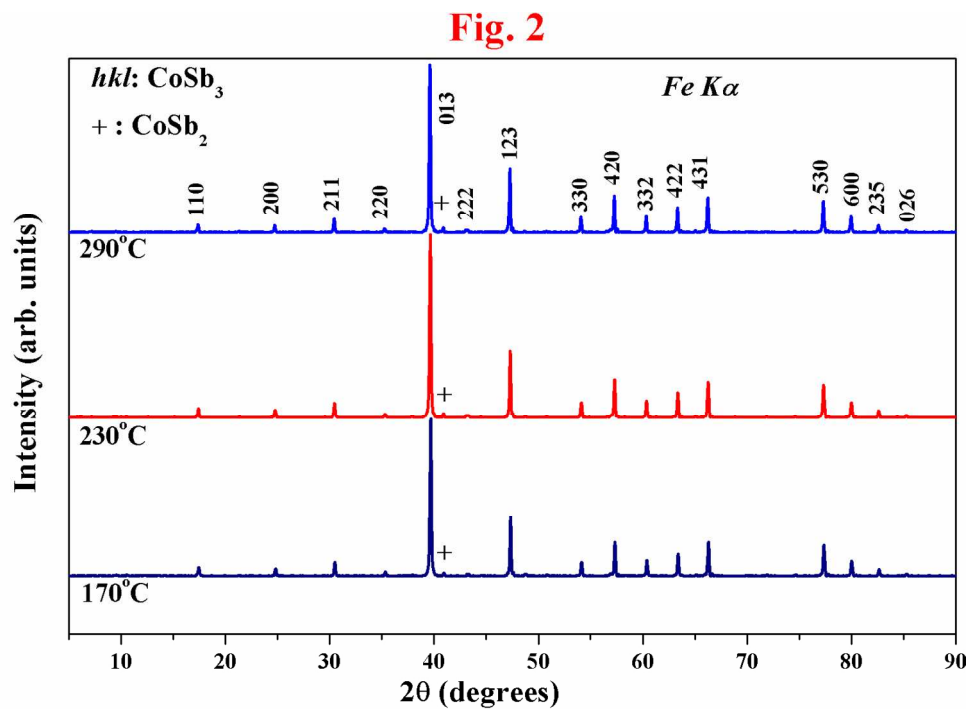
Table I. Room-temperature physical and transport properties for CoSb_3 samples hydrothermally synthesized at various temperatures of 170°C , 230°C and 290°C for 12 h, followed by heating at 580°C for 5 h.

Table II. Some physical properties calculated from curve fitting of electrical conductivity and thermopower of the title CoSb_3 samples in the framework of the Mott's model of variable-range hopping conduction.

Fig. 1

Powder XRD pattern of hydrothermally reacted samples at various temperatures (insets) for 12 h. Herein hkl indices denote CoSb₃ phase, (+), (*), and (\$) symbols represent CoSb₂, CoSb and Sb impurity phases, respectively.

289x203mm (150 x 150 DPI)



Powder XRD patterns of as-hydrothermally reacted samples (Fig. 1) after heating at 580°C for 5 h into evacuated ampoules; thereat *hkl* indices denote CoSb_3 phase and (+) symbol represents CoSb_2 impurity phase.

289x203mm (150 x 150 DPI)

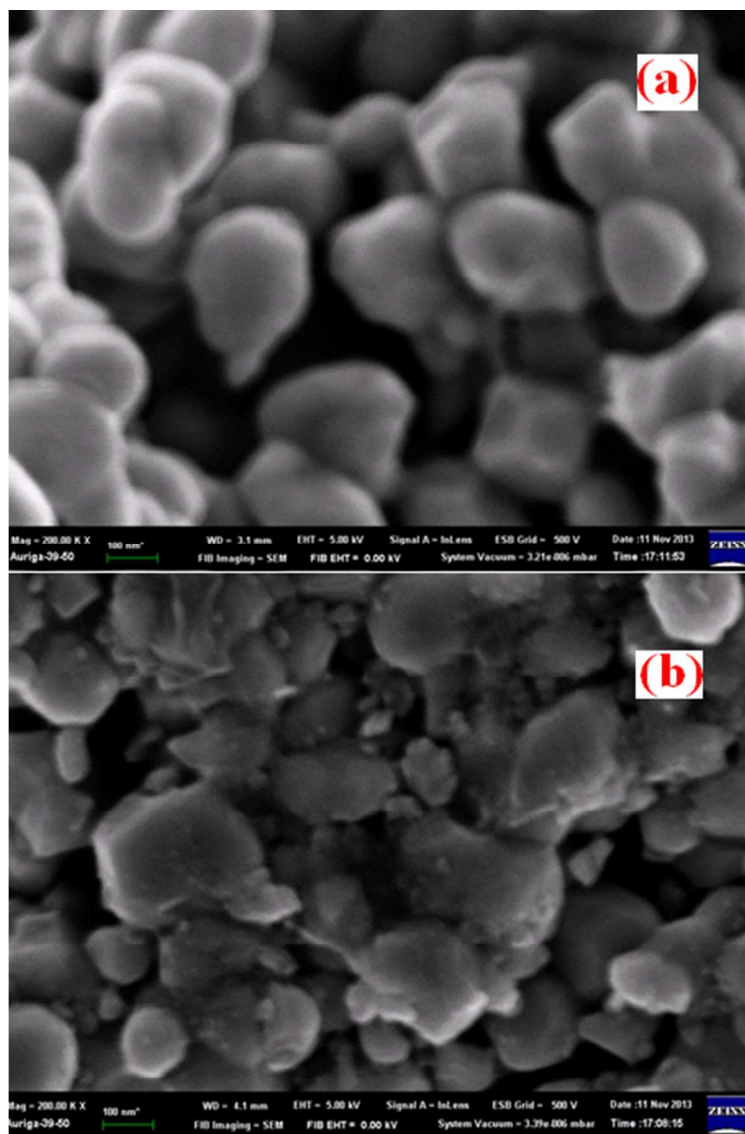
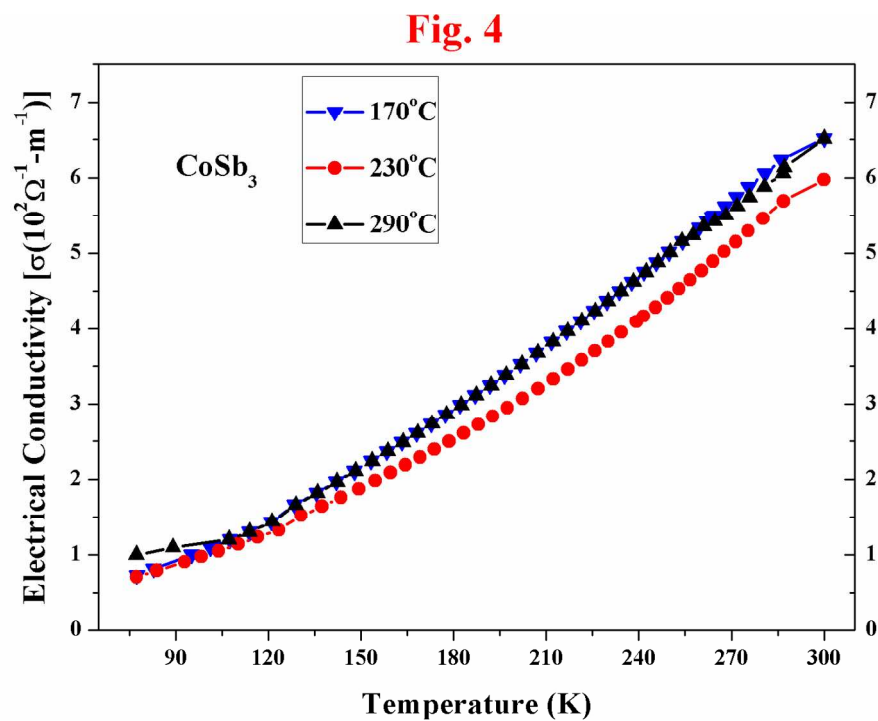


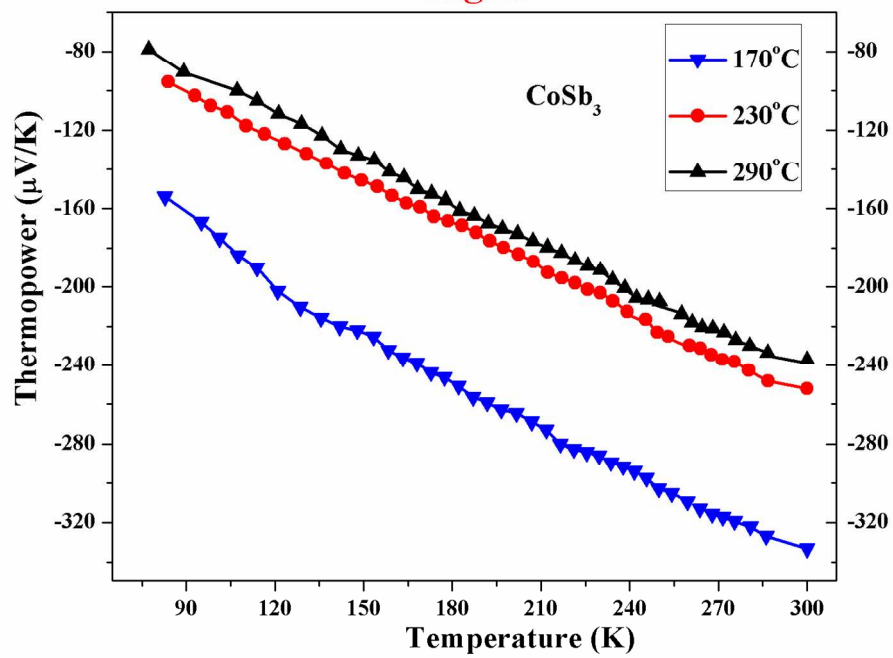
Fig. 3 (a & b)

120x193mm (96 x 96 DPI)



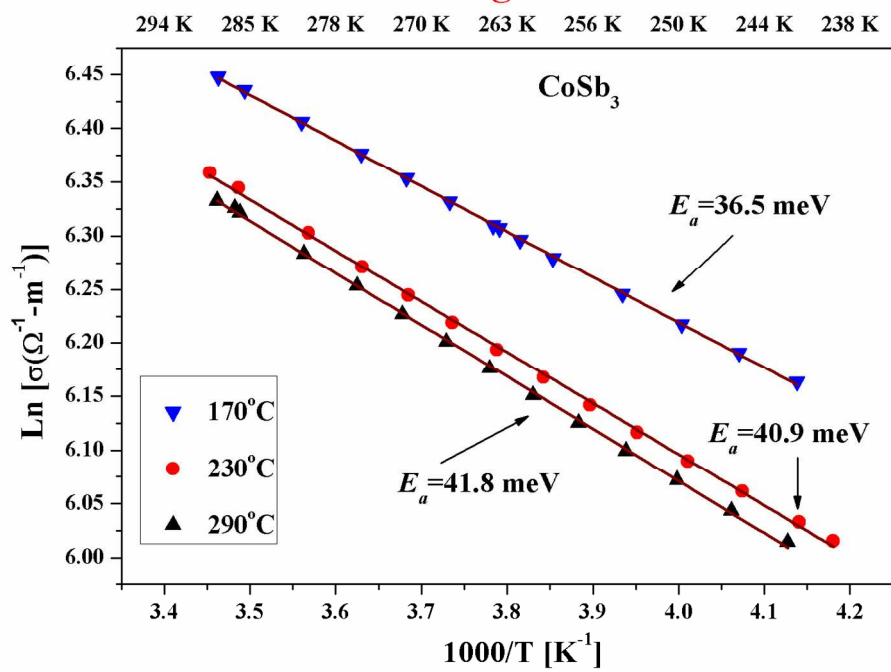
Electrical conductivity of CoSb₃ samples hydrothermally synthesized at various temperatures (inset of figure) followed by heating into evacuated ampoules at 580°C for 5 h.
289x203mm (150 x 150 DPI)

Fig. 5

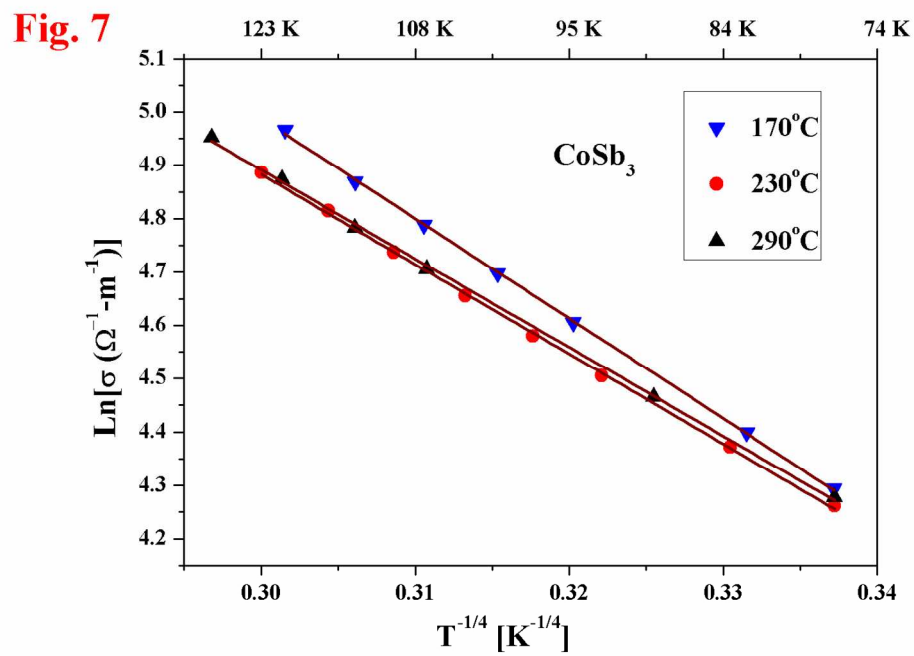


289x203mm (150 x 150 DPI)

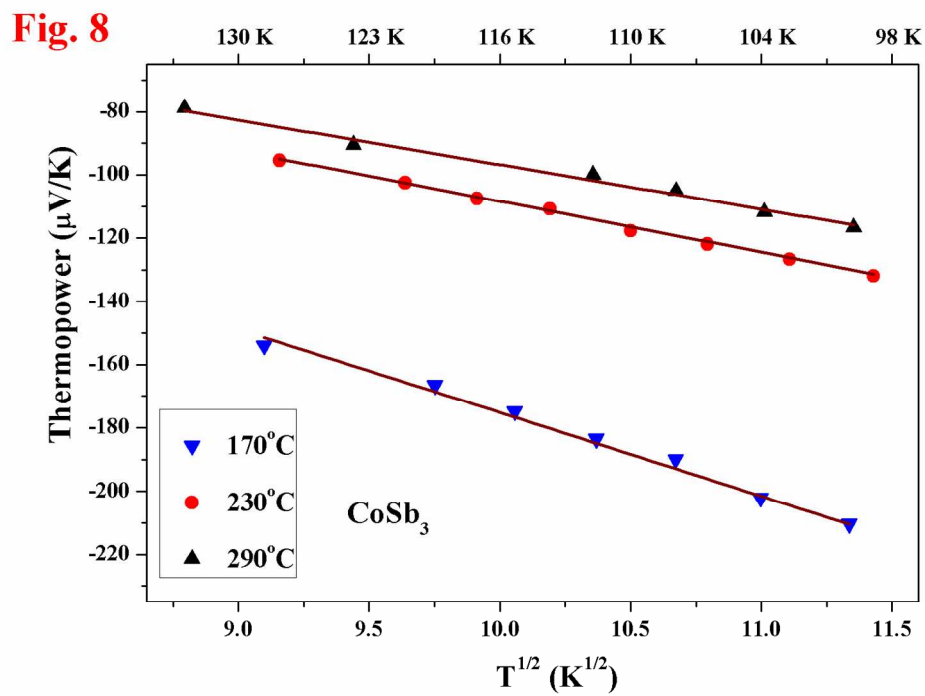
Fig. 6



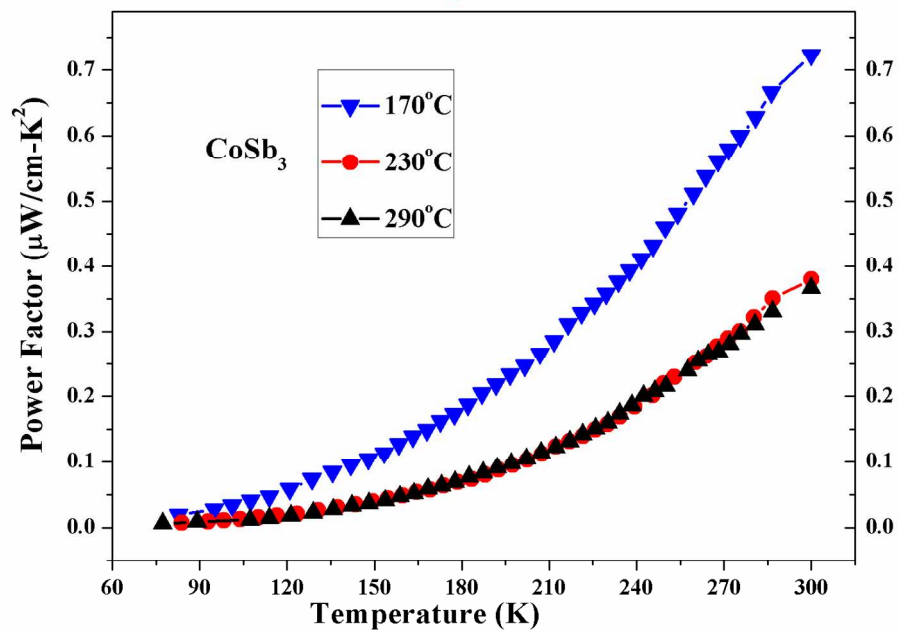
289x203mm (150 x 150 DPI)



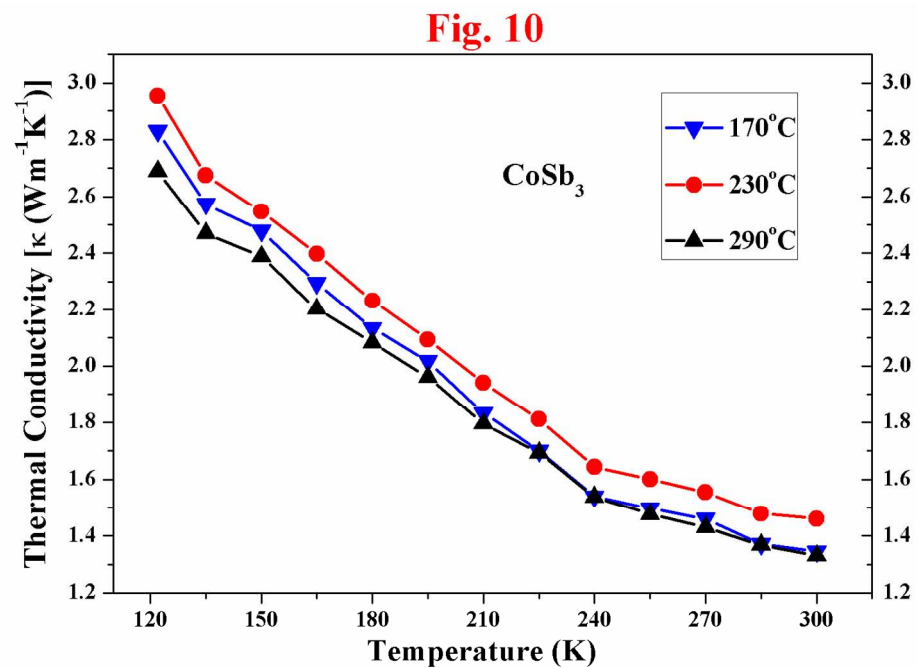
287x201mm (150 x 150 DPI)



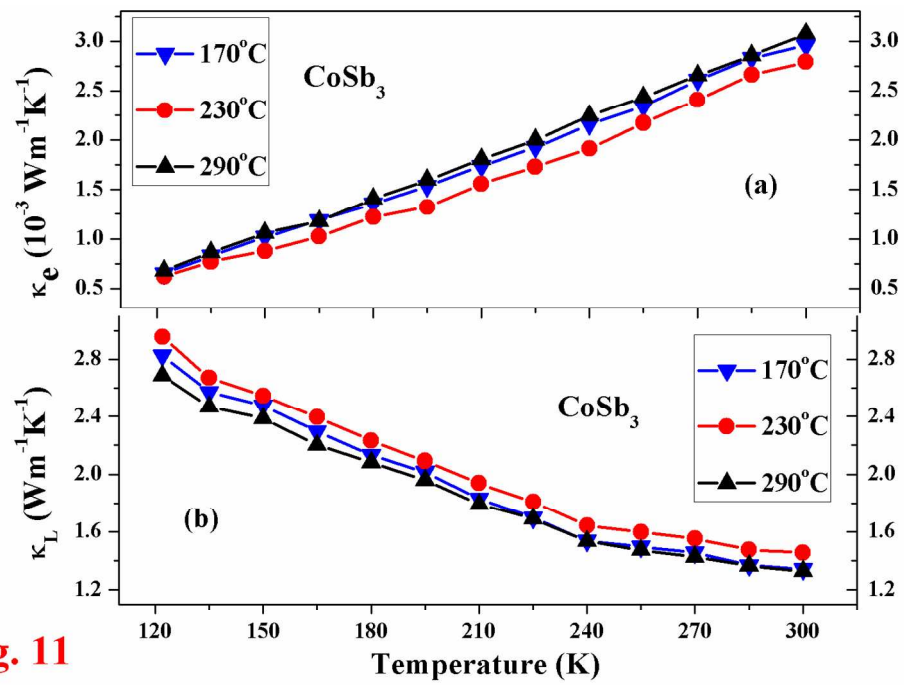
287x201mm (150 x 150 DPI)

Fig. 9

Power Factor for CoSb_3 samples hydrothermally synthesized at various temperatures (inset) followed by heating into evacuated ampoules at 580°C for 5 h.
289x203mm (150 x 150 DPI)

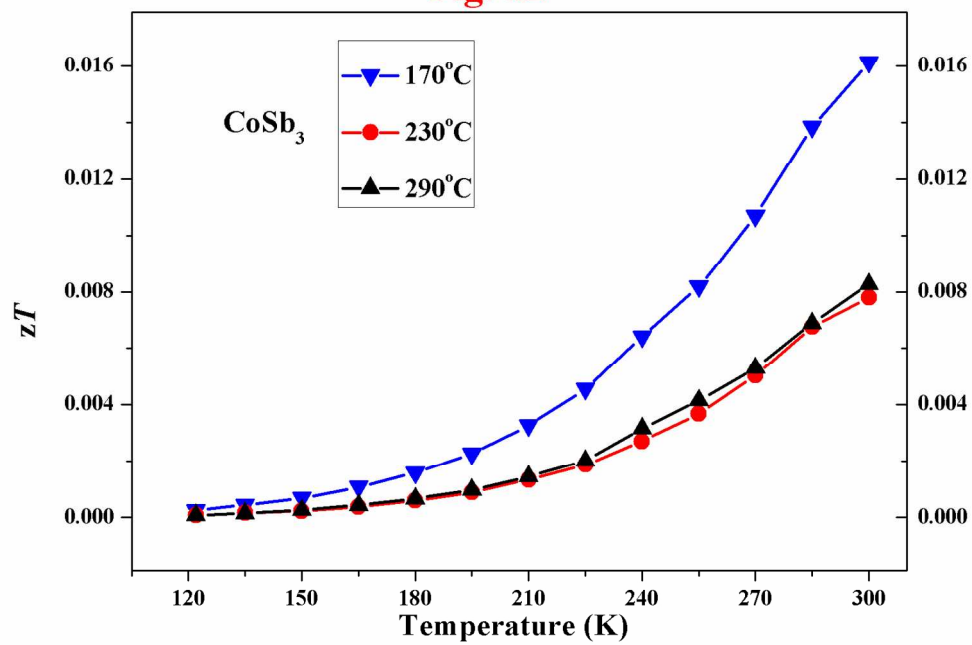


Total thermal conductivity (κ) of CoSb₃ samples hydrothermally synthesized at various temperatures (inset of figure) followed by heating into evacuated ampoules at 580°C for 5 h.
289x203mm (150 x 150 DPI)

**Fig. 11**

289x203mm (150 x 150 DPI)

Fig. 12



289x203mm (150 x 150 DPI)

Table I. Room-temperature physical and transport properties for CoSb₃ samples hydrothermally synthesized at various temperatures of 170°C, 230°C and 290°C for 12 h, followed by heating at 580°C for 5 h.

Property	Units	170°C	230°C	290°C
Lattice constant	Å	9.030	9.0345	9.0386
Relative density (%)	----	70.94	78.01	73.69
Carrier concentration	10 ¹⁸ cm ⁻³	- 4.6	- 8.2	- 9.1
Hall mobility	cm ² /V.s	9.51	6.24	6.27
Electrical conductivity	10 ² Ω ⁻¹ m ⁻¹	6.51	5.97	6.51
Thermopower	μV/K	-333	-252	-237
Lattice thermal conductivity	W/mK	1.342	1.457	1.327
Reduced Fermi level, η	----	-1.8	-0.75	-0.5
Electron effective mass (m^*/m_o)	----	1.112	0.789	0.797
Effective density of states	10 ¹⁹ cm ⁻³	2.94	1.76	1.79
Energy band gap	meV	73	81.8	83.6
Lorenz number, L	$(\frac{k_B}{e})^2$	2.038	2.097	2.119

Table II. Some physical properties calculated from curve fitting of electrical conductivity and thermopower of the title CoSb₃ samples in the framework of the Mott's model of variable-range hopping conduction.

Synthesis temperature (°C)	T ₀ (K)	$W \sim k_B(T_0 T^3)^{1/4}$ (eV) (T=100 K)	$\left[\frac{d \ln N(E)}{dE} \right]_{E=E_F}$ (eV) ⁻¹
170	123266.9	0.051	20.33
230	80564.15	0.046	15.19
290	76549.97	0.045	13.74